Class. Quantum Grav. **17** (2000) 2385–2398. Printed in the UK PII: S0264-9381(00)50380-3

Rotation sensing with a dual atom-interferometer Sagnac gyroscope

T L Gustavson†, A Landragin‡ and M A Kasevich
Physics Department, Yale University, PO Box 208120, New Haven, CT 06520-8120, USA

Received 24 March 2000

Abstract. We reports improvements to our Sagnac effect matter-wave interferometer gyroscope. This device now has a short-term rotation-rate sensitivity of 6×10^{-10} rad s^{-1} over 1 s of integration, which is the best publicly reported value to date. Stimulated Raman transitions are used to coherently manipulate atoms from counterpropagating thermal beams, forming two interferometers with opposite rotation phase shifts, allowing rotation to be distinguished from acceleration and laser arbitrary phase. Furthermore, electronically compensating the rotation-induced Doppler shifts of the Raman lasers allows operation at an effective zero rotation rate, improving sensitivity and facilitating sensitive lock-in detection readout techniques. Long-term stability is promising but not yet fully characterized. Potential applications include inertial navigation, geophysical studies and tests of general relativity.

PACS numbers: 0375D, 0630G, 3280L, 3920, 4250V

(Some figures in this article appear in colour in the electronic version; see `www.iop.org`)

1. Introduction

Gyroscopes based on the Sagnac effect measure a rotation rate relative to an inertial reference frame, based on a rotationally induced phase shift between two paths of an interferometer. Sensitive gyroscopes have potential applications in navigation, geophysics and general relativity. This paper presents improvements to our atom-interferometer gyroscope apparatus, including a factor of 30 increase in short-term sensitivity over our previously published work [1], which now exceeds that achieved by other matter-wave gyroscope experiments by a factor of 6000. Other major improvements include implementation of counterpropagating atomic beams and electronic rotation rate compensation. Preliminary studies of long-term stability are also discussed.

Sagnac effect rotation rate sensors have been constructed using light [2], neutrons [3], neutral atoms [1, 4, 5] and electrons [6]. The phase shift for an interferometer rotating at an angular velocity Ω can be written for either photons or massive particles as follows:

$$\Delta\Phi = \frac{4\pi \boldsymbol{\Omega} \cdot \boldsymbol{A}}{\lambda v}. \tag{1}$$

Here v is the velocity of the particle and λ is its wavelength, which for a massive particle is the de Broglie wavelength $\lambda_{\mathrm{dB}} = h/mv$ (h is Planck's constant and m is the mass of the

---

† Present address: Department of Physics and Research Laboratory of Electronics, Massachusetts Institute of Technology, Cambridge, MA 02139, USA.
‡ Present address: Laboratoire de l'Horloge Atomique, Université Paris XI, Bat. 220, 91405 Orsay Cedex, France.

particle). The phase shift depends on the enclosed area $\boldsymbol{A}$ of the loop but is independent of its shape. Comparing atom- and light-based interferometers with the same area, one finds that the intrinsic sensitivity is larger by a factor of $mc^2/\hbar\omega = 6 \times 10^{10}$ for caesium atoms compared with a HeNe laser, motivating the atom-interferometry approach described here. Indeed, since atom interferometers with spatially separated trajectories were first achieved in 1991, atom interferometry has proven to be a useful precision measurement technique. However, the intrinsic sensitivity advantage of the atom-interferometer gyroscope is diminished by the much larger areas currently obtainable with a light-based interferometer. Better beamsplitters are available for light than for atoms, and the effective area can be increased by high finesse mirrors in a ring-laser gyro or multiple fibre turns in a fibre-optic gyro. Nonetheless, the short-term sensitivity of our atom-interferometer gyroscope is now 6×10^{-10} rad s^{-1} Hz$^{-1/2}$ compared with the 1.3×10^{-9} rad s^{-1} Hz$^{-1/2}$ sensitivity reported for a 1 m^2 ring laser gyroscope [2, 7]. Eventually, advances in atom optics are likely to result in much larger enclosed areas for atom interferometers.

1.1. Outline

The remainder of this paper is organized as follows. Section 2 describes some of the primary applications for high-performance gyroscopes, and section 3 describes the gyroscope interferometer configuration and experimental apparatus used. Section 4 outlines the procedure for calculating interferometer phase shifts, explains the advantages of counterpropagating atomic beams and discusses electronic methods for modulating the effective rotation rate. Synchronous detection techniques and their application to absolute rotation measurements are also discussed. Section 5 characterizes the performance of the apparatus. It describes short-term sensitivity and signal-to-noise ratio, systematic errors (and reduction thereof), and preliminary long-term stability results. Finally, section 6 gives a summary and discusses possible plans for the future.

2. Applications

One application for sensitive gyroscopes is inertial navigation, which is the determination of the current position relative to a known starting point through the continual monitoring of angular orientation and accelerations without referring to external landmarks. Accurate gyroscopes and accelerometers are required because small measurement errors can quickly become large position errors. Inertial navigation systems can be used to supplement the global positioning system (GPS) as well as for applications for which GPS is impractical (for example, due to poor satellite visibility).

Geophysicists are interested in precise rotation sensors for studying rotational motion of tectonic plates during seismic events. In addition, improved models of the Earth's composition and dynamics may result from studying variations in the Earth's rotation rate that are on the order of $\sim 10^{-8}\Omega_{\mathrm{E}}$ on time scales of a few days. Here $\Omega_{\mathrm{E}} \simeq 7.292 \times 10^{-5}$ rad s^{-1} is the rotation rate of the Earth about its axis. Furthermore, local measurements made by gyroscopes would complement the distributed measurements made by very-long baseline interferometry (VLBI).

Torsion pendulum measurements of the gravitational constant G may ultimately be limited by knowledge of local rotational noise from seismic and cultural sources [8]. Rotational noise at the pendulum oscillation rate (typical periods are between 100 and 1000 s) will give a systematic offset in the determination of G, which potentially could be corrected using a gyroscope like the one described here.

To test general relativity, one could measure the precession of a gyroscope (defining a locally non-rotating reference frame) relative to a reference frame defined by the distant stars. This precession arises from parallel propagating a vector through curved spacetime around a massive rotating body such as the Earth, and therefore applies equally to different types of gyroscopes. The effect can be divided into two parts: the geodetic effect is due to motion around a massive body that is not rotating, and the Lense–Thirring effect [9] arises due to the rotation of a massive body. For a gyroscope in orbit, the total precession rate is given by the sum of the two effects

$$\boldsymbol{\Omega}_{\mathrm{geo}} = \frac{3}{2}\frac{GM}{c^2 r^3}(\boldsymbol{r} \times \boldsymbol{v}) \tag{2}$$

$$\boldsymbol{\Omega}_{\mathrm{LT}} = \frac{GI}{c^2 r^3}\left[\frac{3\boldsymbol{r}}{r^2}(\boldsymbol{\omega} \cdot \boldsymbol{r}) - \boldsymbol{\omega}\right], \tag{3}$$

where $\boldsymbol{\Omega}_{\mathrm{geo}}$ and $\boldsymbol{\Omega}_{\mathrm{LT}}$ are the geodetic and Lense–Thirring precessions, respectively; $\boldsymbol{r}$ and $\boldsymbol{v}$ are the current position and velocity of the gyroscope; M, I, and $\boldsymbol{\omega}$ are the mass, moment of inertia and rotation rate of the Earth. For a 650 km polar orbit around the Earth, one finds $\boldsymbol{\Omega}_{\mathrm{geo}} = 1 \times 10^{-12}$ rad s^{-1} and $\boldsymbol{\Omega}_{\mathrm{LT}} = 6.45 \times 10^{-15}$ rad s^{-1}. The Lense–Thirring effect has recently been measured to 20% precision by Ciufolini *et al*, as described in [10] and elsewhere in these proceedings. The effect was observed by monitoring the orbital parameters of two satellites in polar orbits, and data extraction required detailed modelling of the Earth's mass distribution and gravitational field. The Gravity Probe B (GPB) satellite gyroscope test is designed to measure the geodetic effect to one part in 10^4 and the Lense–Thirring effect to within 2% [11]. GPB will measure the precession of spinning superconducting spheres in a cryogenic environment within a drag-free satellite†. Measuring the Lense–Thirring effect tests a unique aspect of general relativity, and might prove to be one of only a few tests that are within experimentally achievable limits. Because the atom-interferometer sensitivity improves as the interferometer length squared, a large instrument could make a ground-based test of general relativity feasible [13]. For example, increasing the length of our present 2 m long apparatus by a factor of 10 should yield a 100-fold improvement in sensitivity.

3. Apparatus

Much of our apparatus has been described previously. Results obtained with a single atom-interferometer configuration are presented in [1], implementation of dual counter-propagating interferometers and improved atomic sources are described in [14] and a detailed treatment including our most recent work is given in [15]. A schematic view of the gyroscope apparatus interferometer configuration is shown in figure 1, and a brief description follows.

Two-photon stimulated Raman transitions are used as beamsplitters and mirrors to manipulate atoms [16, 17]. Two counterpropagating laser beams are required, with a frequency difference equal to the hyperfine splitting of the caesium $6\mathrm{S}_{1/2}$ ground states ($F = 3$ and 4), namely the clock transition at 9.2 GHz. The transition produces a change of internal state accompanied by a corresponding momentum kick of $\hbar\boldsymbol{k}_{\mathrm{eff}}$, where $\boldsymbol{k}_{\mathrm{eff}} = \boldsymbol{k}_1 - \boldsymbol{k}_2$. Both lasers are detuned ~ 2 GHz from the atomic resonance with the $6\mathrm{P}_{3/2}$ excited state, avoiding

---

† Since the GPB readout is expected to be limited by the shot noise of the readout current, its ability to determine angle improves like $t^{1/2}$. However, if the instrument is used to measure a constant rotation rate, then the angular displacement increases linearly with time. This leads to a rotation rate measurement that improves like $t^{3/2}$ for GPB, in contrast to the $t^{1/2}$ scaling of a shot-noise-limited Sagnac gyroscope. GPB has an expected sensitivity of 1 marcsec (4.85×10^{-9} rad) over a 4 h integration [12]. That implies an angle measurement of 5.8×10^{-7} rad in 1 s (or $\simeq 5.8 \times 10^{-7}$ rad s^{-1}), which is 970 times worse than the Yale gyro, but in 4 h, GPB should achieve 3.4×10^{-13} rad s^{-1}, which is 15 times better than the scaled Yale gyro performance.

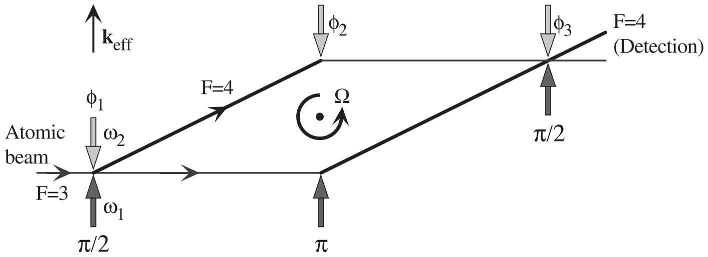

Figure 1. Interferometer configuration. Three pairs of Raman beams are used to divide, deflect and recombine atomic trajectories.

spontaneous emission. For Raman transitions, the RF laser frequency difference must be stable, but highly stable individual lasers are not required. Light beamsplitters for atoms have the advantage over mechanical gratings that they are more easily vibrationally isolated and do not clog. Because Raman beamsplitters transfer atoms between different ground states, a highly collimated atomic beam is not required as is the case for mechanical gratings or diffraction from standing waves, where diffracted orders must be resolved to distinguish a signal from background atoms. A disadvantage of Raman transition beamsplitters is that AC Stark shifts of the atomic energy levels due to off-resonant laser light can cause spurious interferometer phase shifts. Techniques used to minimize these shifts are described in section 5.2.

We generate the Raman laser frequencies from a master diode laser by using an acousto-optic modulator (AOM) operating at 4.6 GHz, and amplify the ±1 diffraction orders by optical injection locking slave diode lasers [18]. Light from the two Raman lasers is combined with crossed polarizations on a beamsplitter cube and copropagates throughout the apparatus. The light is spatially filtered and then divided into three Raman pulses using plate beamsplitters. Raman transitions between copropagating beams (Doppler-insensitive configuration) are suppressed because the Raman detuning $\delta_{12} = \omega_1 - \omega_2$ is 160 MHz from the Raman transition resonance. After the Raman beams exit the vacuum chamber, the light is retroreflected through an AOM such that one pair of counterpropagating beams (Doppler-sensitive configuration) is on resonance.

To form the interferometer, a horizontal thermal beam of caesium atoms is transversely cooled and optically pumped into the $F = 3$ ground state before passing into a magnetically shielded interferometer region within a UHV vacuum chamber. The atoms pass through a sequence of three Raman laser interaction regions, with the lasers in a horizontal plane perpendicular to the atomic beam. The first beam ($\pi/2$) puts the atoms in a coherent superposition of the $F = 3$ and 4 ground states. This first pulse serves as a beamsplitter, causing the atomic wavepackets to divide into two trajectories. The second beam (π) acts as a mirror, exchanging the atomic states and momenta and deflecting the trajectories back towards each other. The third beam ($\pi/2$) acts as a beamsplitter and recombines the trajectories, forming a Mach–Zehnder-type interferometer. (The $\pi/2$–π–$\pi/2$ interferometer sequence we use is similar to that used to measure gravitational acceleration by Kasevich and Chu [19, 20], except that our interferometer uses spatially separated pulses rather than pulses in the time domain.) Rotation induces a phase shift between the two arms of the interferometer, and the interference signal is observed by measuring the number of atoms in the $F = 4$ state using a probe laser tuned to resonance and imaging the atomic fluorescence onto a photodiode. A magnetic bias field along the axis of the Raman beams shifts the transition frequencies corresponding to the different Zeeman m_F sublevels such that only the magnetic field insensitive $m_F = 0$ atoms are resonant with the Raman transitions and participate in the interferometer, minimizing phase shifts due to inhomogeneities in the magnetic field.

4. Interferometer phase shifts

References to several viewpoints for calculating the Sagnac effect can be found in [2, 21]. The calculation may be performed in either the laboratory frame or in an inertial frame, as well as for time-domain or spatial-domain beamsplitters. Bordé *et al* have studied the theory of spatial-domain beamsplitters in detail (including effects of finite pulse width, which have been neglected here) in [22, 23] and references therein. To derive the interferometer phase shift, it is convenient to treat spatial propagation through the interferometer and interactions with the Raman lasers separately. The phase shift for our interferometer configuration was computed using this approach in [24], and a similar configuration was treated previously in [25]. Only a rough outline of the calculation will be presented here.

The spatial propagation phase shift can be computed using path integrals [26] of the Lagrangian. In classical mechanics, Hamilton's principle of least action states that a particle moving in an external potential $V(\boldsymbol{r})$ will travel along the path for which the integral

$$S_\Gamma \equiv \int_{t_a}^{t_b} L[\boldsymbol{r}(t), \dot{\boldsymbol{r}}(t)]\,\mathrm{d}t \tag{4}$$

is stationary, where the Lagrangian is defined as $L[\boldsymbol{r}, \dot{\boldsymbol{r}}] \equiv \frac{1}{2}m\dot{\boldsymbol{r}}^2 - V(\boldsymbol{r})$, and S_Γ is the *action* along the path Γ. Stationary means that the integral is extremal with respect to small variations in the path, that is, $\delta S_\Gamma = 0$. The classical action is denoted by

$$S_{\mathrm{cl}} \equiv S_{\mathrm{cl}}(\boldsymbol{r}_b, t_b; \boldsymbol{r}_a, t_a), \tag{5}$$

and represents the action evaluated along the classical path between the endpoints a and b, depending only on the endpoints. In our interferometer, atoms are treated classically with position and velocity corresponding to the centre of mass and group velocity of a spatially localized quantum mechanical wavepacket. The phase accumulated due to propagation between two points is

$$\Delta\phi = S_{\mathrm{cl}}/\hbar. \tag{6}$$

The phase shift due to a perturbation to the Lagrangian ΔL can be calculated to first order by integrating the perturbing potential over the unperturbed classical path, Γ_0. Therefore, the phase difference between the two interferometer arms is given by

$$\Delta\Phi = \frac{1}{\hbar}\oint_{\Gamma_0} \Delta L\,\mathrm{d}t. \tag{7}$$

In the rotating frame, Coriolis acceleration adds a perturbation $\Delta L = m\boldsymbol{\Omega}\cdot(\boldsymbol{r}\times\boldsymbol{v})$ to the free-particle Lagrangian.

The phase shift due to interaction with the laser light can be derived from the solution of the Raman transition equations given, for example, in [17]. At each vertex of the interferometer diagram corresponding to the atom receiving a momentum kick, an appropriate phase factor must be applied, namely

$$\exp(\pm\mathrm{i}[\boldsymbol{k}_{\mathrm{eff}}\cdot\boldsymbol{x} - (\omega_{\mathrm{eff}} - \omega_{eg} - \omega_r)t_0 - \phi_{\mathrm{eff}}]), \tag{8}$$

where $\omega_{\mathrm{eff}} = \omega_1 - \omega_2$, ω_{eg} is the caesium hyperfine splitting frequency, $\omega_r = \hbar k_{\mathrm{eff}}^2/2m$ is the recoil frequency, and the factor $\mathrm{e}^{\mathrm{i}\boldsymbol{k}_{\mathrm{eff}}\cdot\boldsymbol{x}}$ corresponds to the momentum of the absorbed photon. The arbitrary phase ϕ_{eff} is given by the difference of the individual Raman laser arbitrary phases, evaluated at the point of interaction with the atoms.

Our atom interferometer is sensitive to linear or Coriolis acceleration $\boldsymbol{a}$ along the Raman beam axis. Combining the phase shifts for spatial propagation and laser interactions, it can be shown that the total interferometer phase shift is

$$\Delta\Phi = -\boldsymbol{k}_{\text{eff}} \cdot \boldsymbol{a}\frac{L^2}{v^2} + \phi_1 - 2\phi_2 + \phi_3, \tag{9}$$

where ϕ_j represents the arbitrary phase from the jth Raman beam (evaluated at the point of interaction with the atoms). For rotation, $\boldsymbol{a}$ is the Coriolis acceleration

$$\boldsymbol{a}_{\text{Cor}} = -2\boldsymbol{\Omega} \times \boldsymbol{v}. \tag{10}$$

4.1. Counterpropagating atomic beams

Because the rotation phase shift depends on the Coriolis acceleration and thus the vector velocity, reversing the direction of the atomic beam yields a rotation phase shift with opposite sign. Our rotation rate measurement approach depends fundamentally on this phase shift reversal.

In the limit of perfect contrast, the probability for an atom exiting the interferometer in the $F = 4$ state used for detection is equal to

$$P(F = 4) = \tfrac{1}{2}[1 - \cos(\Phi_\Omega + \phi_{\text{arb}})], \tag{11}$$

where Φ_Ω is the Sagnac phase shift, and $\phi_{\text{arb}} = \phi_1 - 2\phi_2 + \phi_3$ is the sum of acceleration and the arbitrary laser phase. Therefore, the gyroscope signals corresponding to counterpropagating atomic beams have the form

$$S_{\text{north}} \sim \cos(\Phi_\Omega + \phi_{\text{arb}}) \tag{12}$$

$$S_{\text{south}} \sim \cos(-\Phi_\Omega + \phi_{\text{arb}}), \tag{13}$$

where S represents the detected signal of the north or south atomic beam (north and south are arbitrary labels for the counterpropagating atomic beams), and Φ_Ω represents the Sagnac phase shift. Using trigonometric identities, one can rearrange these equations as follows:

$$S_{\text{north}} - S_{\text{south}} \sim \sin(\Phi_\Omega)\cos(\phi_{\text{arb}}). \tag{14}$$

Due to the sine factor, the difference signal has a zero crossing for zero rotation rate, and the amplitude factor (cosine) can be maximized by adjusting the arbitrary phase. Therefore, this method allows precise determination of the zero rotation rate relative to the non-rotating inertial frame, and does not depend on knowledge of the gyroscope area or arbitrary phase.

To implement the counterpropagating atomic beams, caesium sources were mounted at each end of the vacuum chamber and aligned to overlap spatially so that the beams would sample the same magnetic bias field (collisions are negligible). The atoms from each atomic beam are transversely cooled in two dimensions using red-detuned laser light, and are optically pumped into the $F = 3$ ground state before passing through the detection laser for the opposing atomic beam. Since the detection light is tuned to the $F = 4 \rightarrow F' = 5$ resonance, the only atoms detected are those that end up in the $F = 4$ state after the interferometer interaction pulses. To enhance common-mode rejection, the interferometers share all laser sources, including light for state preparation, Raman beams and detection.

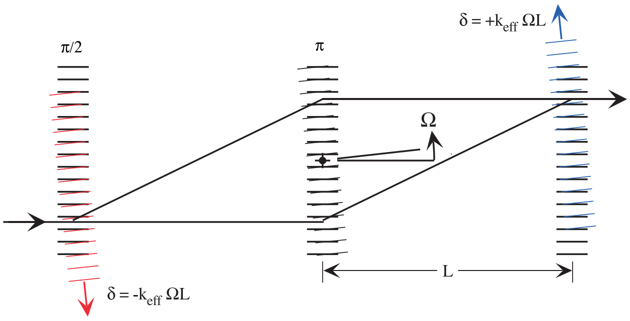

Figure 2. Rotation-induced Doppler shifts. The wavefronts of the three Raman pulses are drawn in their initial positions and after rotation of the apparatus about the centre of the π pulse. Small rotations leave the π pulse essentially unchanged, but Doppler shift the $\pi/2$ pulses by $\pm k_{\mathrm{eff}}\Omega L$. For clarity, only one Sagnac loop has been drawn, but the shifts are the same for each. The wavefronts and Sagnac loop are not drawn to scale.

4.2. Doppler shifts

In an inertial frame, rotation about the centre of the π pulse appears as a Doppler shift of the $\pi/2$ beams of magnitude

$$\delta = k_{\mathrm{eff}}\Omega L, \tag{15}$$

with opposite signs for the north and south $\pi/2$ beams. Figure 2 illustrates the Doppler shifts due to rotation. The interferometer phase shift can be interpreted as arising from the rotation induced Doppler shifts, and can be shown (to a first-order approximation) to result in a phase shift of

$$\Delta\Phi \simeq 2\delta L/v = 2k_{\mathrm{eff}}\Omega L^2/v, \tag{16}$$

where v is the longitudinal velocity of the atomic beam. The Earth's rotation rate causes a Doppler-shift of $\delta f = \delta/2\pi = 108.8$ Hz for our horizontally oriented instrument at Yale's latitude, measured by GPS to be 41:19:02.661N ($\sin(\phi_{\mathrm{lat}}) = 0.660$). The single interferometer phase shift due to the Earth's rotation rate would be 6.8 rad, and the projection at Yale's latitude is 4.5 rad.

4.3. Electronic rotation compensation

The AOMs used in the Raman beam retroreflections make it possible to tune the Raman transition frequency independently for each of the three pulses. In particular, shifting the frequencies of the $\pi/2$ beams by $\pm\delta f = 108.8$ Hz compensates for the Doppler shifts induced by the rotation rate of the Earth, described in the previous section. Because the Doppler shift depends only on the interferometer geometry and laser wavelength, the compensation works for both atomic beams and is independent of the velocity distribution of the atoms. To calibrate the frequency shifts in terms of rotation rate, we measured the separation between Raman beams, $L = 96.842 \pm 0.015$ cm, using a pinhole attached to a precision caliper. With the DC rotation compensated, we recover the maximum fringe contrast—as obtained for zero rotation rate in the absence of compensation. The contrast decreases for non-zero rotation rates due to averaging over longitudinal velocities in the atomic beam, since the phase shift depends on the velocity.

Rather than simply cancelling the bias due to the Earth's rotation rate, one could servo δf so that the rotation signal always reads zero, and accurately determine the rotation rate from the frequency offset δf. A closed loop rotation readout could improve the instrument's linearity by ensuring that the gyroscope is always operating near an effective zero rotation rate. Also, the dynamic range of measurable rotation rates could be increased, since servoing δf would keep the signal within the contrast envelope even for large rotation rates.

To avoid introducing unnecessary phase noise when adding the AOMs in the Raman retroreflections, the frequency-shifted light in the Raman retroreflection was phase-locked to the unshifted light (compared as close to the vacuum chamber as possible). This was accomplished by comparing the ~160 MHz beatnote on a photodiode with a stable RF reference and servoing the AOM frequency using a voltage-controlled oscillator (VCO). A separate phase-locked loop is required for each of the three Raman retroreflection beams.

4.4. Frequency modulation

The electronic rotation compensation scheme described above can also be used to simulate the rotation of the optical table by scanning δf, avoiding the vibration and calibration uncertainties of mechanically rotating the table. (Previously, we had rotated the table with a piezo-electric transducer attached to a vibration-isolated massive column, and measured the velocity with a seismometer.) We also implemented a frequency modulation detection scheme in which we scanned δf with a triangle modulation which spanned the entire contrast envelope, acquiring multiple samples per scan. The rotation phase shift was computed for each scan after using a nonlinear curve-fitting routine to fit the data from both atomic beams. Such synchronous detection schemes are useful for reducing sensitivity to technical noise outside the modulation frequency band (for example, variations in atomic flux). To minimize phase noise, a single RF synthesizer was used to sweep $+\delta f$ or $-\delta f$ for the two $\pi/2$ beams, and this synthesizer output was mixed with two additional synthesizers to generate the RF references for each of the three Raman retroreflections. The synthesizers were combined in a symmetric fashion that exploited the interferometer laser arbitrary phase dependence $\phi_1 - 2\phi_2 + \phi_3$ such that slow phase drifts of any synthesizer cancelled in the interferometer signal.

4.5. Phase modulation

Adding a frequency offset to the π Raman beam causes the interferometer phase shift to increase linearly in time, which means that the number of atoms detected in the $F = 4$ state oscillates sinusoidally in time (see equation (11)). This can be seen in the time-domain picture by substituting the appropriate frequencies and times for the Raman laser arbitrary phases. Suppose the $\pi/2$ Raman lasers are at frequency ω_{eff}, the π pulse is at frequency $\omega_{\text{eff}} + \epsilon$, and an atom entering the interferometer at time t_0 takes a time $T = L/v$ to travel the distance L between pulses. Then we find

$$\Delta\Phi = \phi_1 - 2\phi_2 + \phi_3 = \omega_{\text{eff}} t_0 - 2(\omega_{\text{eff}} + \epsilon)(t_0 + T) + \omega_{\text{eff}}(t_0 + 2T) \tag{17}$$

$$= -2\epsilon t_0 - 2\epsilon T. \tag{18}$$

The first term of equation (18) increases linearly with time, and the second term corresponds to a constant acceleration. We used modulation frequencies between 3 and 48 Hz with 10 samples per period and determined the phase by fitting the sine waves using a nonlinear curve-fitting routine as a post-processing step. By subtracting and adding the phase for the north and south atomic beams, we recovered the rotation phase (modulo 2π) and the arbitrary phase (including acceleration). This linear phase modulation technique proved to be a convenient and robust

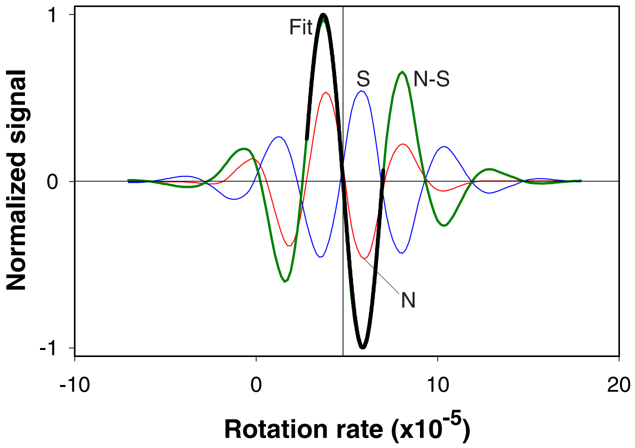

Figure 3. Earth rotation rate measurement (preliminary). The north and south rotation fringes are the symmetric signals shown with thin curves, the difference north − south is labelled N-S, and the fit to the centre of the difference curve is shown with a heavy black curve. The arbitrary phase was chosen so that the north and south signals have opposite sign, maximizing the contrast of the difference signal. From the fit, we determine $\Omega_E = 7.24 \times 10^{-5}$ rad s^{-1} (after compensating for latitude).

way to acquire rotation rate data. By combining four RF synthesizers, we were able to add an offset ϵ to the π pulse or shift the $\pi/2$ pulses by δf for electronic rotation compensation and modulation. However, the low-frequency phase noise does not cancel for the four-synthesizer configuration as it did for the frequency modulation scheme.

4.5.1. Earth rotation measurement. To test the technique of using the difference between the north and south atomic beams to determine the absolute rotation zero, we measured the Earth rotation rate. We used the frequency modulation technique to electronically scan the effective rotation rate. The Doppler shift correction frequency δf was swept 400 Hz over 10 s, and the signal was phase modulated at 48 Hz so lock-in demodulation could be used for detection. The results are shown in figure 3. The time-varying frequency shift δf was converted to an equivalent rotation rate based on the Doppler shift, using equation (15). We took the difference of the north and south normalized signals, and fit the centre of the curve to a sine wave. The point where the fitting curve crossed $y = 0$ was determined to be the zero rotation rate. (At this point, δf cancelled the Earth rotation rate.) We measured the Earth rotation rate to be $\Omega_E = 7.24 \times 10^{-5}$ rad s^{-1}, after correcting for Yale's latitude, compared with the expected value of $\Omega_E = 7.29 \times 10^{-5}$ rad s^{-1}. The dominant source of error was AC Stark shifts due to Raman laser misalignment. This and other systematic effects are discussed in section 5.2 along with experimental modifications that have dramatically reduced susceptibility to systematic errors.

5. Performance and results

This section discusses the performance of the instrument in different regimes. Short-term sensitivity measures the ability to detect small rotations over short time scales for which slow drifts of the apparatus are unimportant, and depends on interferometer area and signal-to-noise ratio. We used a rotation-independent method to determine the signal-to-noise ratio because we have no independent means to characterize the rotational noise of the laboratory, which we expected to be above the intrinsic sensitivity of the gyroscope. Gyroscope test facilities exist; however, the difficulty of transporting our current apparatus precluded their use. For long-term stability, dimensional stability of the apparatus and pointing stability of the laser beams are critical, though stability is greatly improved by the use of counterpropagating atomic beams. Nonetheless, common-mode rejection cannot completely remove the effect of dimensional drift (i.e. thermal expansion) to the extent that it occurs during the time of flight of the atoms.

5.1. Short-term sensitivity

The improvement in short-term sensitivity over our previous work came from several factors. First, the atom flux was increased from 6×10^8 to 1×10^{11} atom/s (detected in the interferometer region after transverse cooling) by replacing the caesium sources with a recirculating design and increasing the nozzle aperture to 4.5 mm diameter. The most probable velocity of the detected atoms was 290 m s^{-1}, with a transverse velocity spread of ± 10 cm s^{-1} after transverse cooling. Second, the Raman transition linewidth was broadened by using spatially narrower Raman beams, resulting in ~ 5 times more atoms participating in the interferometer due to the wider range of transverse velocities addressed. Cylindrical optics were added to reshape the Raman beams, resulting in a beam size of 0.5 mm horizontally by 1.5 cm vertically ($1/e^2$ radius beam waist) at the plane of the atomic beams. Third, the detection noise for the atomic beam was reduced by narrowing the linewidth of the master laser diode used to derive the frequencies for transverse cooling and detection (referenced to a caesium vapour cell by saturated absorption). To narrow the linewidth, the distributed Bragg reflector (DBR) master laser with 3 MHz linewidth was optically injection locked to light from a grating-stabilized diode laser with 200 kHz linewidth. Retroreflecting the detection probe beam was found to prevent atoms from acquiring a net transverse momentum change during the detection pulse that would Doppler-shift the atoms off resonance. Keeping the atoms resonant with the probe light reduced the sensitivity to frequency fluctuations of the detection laser. Finally, sensitivity to air current fluctuations was reduced by placing tubes around cooling and detection beams, and building an enclosure around the optical table. To reduce the effect of air currents and mirror vibrations on the Raman beams, the Raman lasers were reconfigured to be copropagating as described in section 3.

We used two techniques to measure the interferometer signal-to-noise ratio independently from the rotational noise of the laboratory. First, we used the electronic rotation compensation technique of section 4.3 to set the effective rotation rate outside the bandwidth of the instrument, in the flat tails of the contrast envelope where there is no rotation sensitivity. We measured a signal-to-noise ratio of 33 000:1 for 1 s of integration, from which we determine a short-term sensitivity of 6×10^{-10} rad s^{-1} Hz$^{-1/2}$, or $8 \times 10^{-6}\Omega_E$. Second, we reconfigured the interferometer to have drastically reduced enclosed area. By using copropagating Raman beams (rather than counterpropagating ones as in the gyroscope configuration), the interferometer enclosed area and sensitivity to rotation and acceleration are reduced by a factor of $k_{\text{eff}}/k_{\text{RF}} \simeq 1.3 \times 10^{-5}$. However, the sensitivity to many other sources of technical noise is unchanged; for example, phase shifts due to Zeeman shifts from changing magnetic fields, Raman pulse area or phase fluctuations, atomic beam flux and AC Stark shifts. With the null-area configuration, we obtained a signal-to-noise ratio of 50 000:1. Note that for both of the above techniques, we used a lock-in amplifier to remove low-frequency drifts by demodulating at 30 Hz, as we would have done in a rotation sensitive geometry. We compared the power spectral densities of the null-area interferometer with that of a single π pulse to measure the phase noise added by the interferometer sequence. The interferometer noise spectrum (including rotation, acceleration and technical noise) had a minimum at about 3 Hz, which we subsequently used as the modulation frequency when doing long-term stability measurements, for which a high-frequency response is unnecessary.

5.2. Systematics

We investigated the sensitivity of the apparatus to possible sources of spurious phase shifts by acquiring dual-interferometer data using the phase modulation technique (described in section 4.5) while varying different parameters. First, we studied the stability of the applied magnetic bias fields, including the interferometer bias and the Helmholtz coils used to cancel the magnetic field in the cooling regions. In the worst case, we measured a phase shift of $\leqslant 3 \times 10^{-5}\Omega_{\mathrm{E}}$ mA^{-1}, and since the current supplies have 7×10^{-3} mA RMS ripple in 1 s, the bias field stability is not a limitation.

Next we studied the sensitivity to the detuning of the free-running Raman master laser, which could cause a phase shift due to changes in the AC Stark shift. We measured a phase-shift dependence of $3 \times 10^{-5}\Omega_{\mathrm{E}}$ MHz^{-1}, which indicated that a servo lock was needed for the master laser frequency. We used a high-speed counter interfaced to a computer to monitor a 2 GHz beatnote between the master Raman laser and the detection laser, which is locked to the $F = 4 \rightarrow F' = 5$ transition, and controlled the master laser current with a digital servo. The locked master laser had a 1.2 MHz RMS frequency error in 1 s, but because the detuning fluctuations are at high frequency and the average is locked precisely, detuning fluctuations are no longer a concern for long-term data acquisition.

The parameter that caused the largest systematic shifts was the horizontal overlap of the Raman beams, causing a phase shift of 1 rad for 100 μm relative displacement, which could occur due to beam-pointing instabilities or imperfect alignment through the spatial filter. To solve this problem, both lasers were coupled into one polarization-maintaining fibre. The fibre enforced spatial overlap between the Raman beams and reduced phase drift due to alignment-dependent AC Stark phase shifts. A Raman laser intensity servo was added to stabilize the power of the two lasers after exiting the fibre, preventing fluctuations due to etalon effects within the fibre. We retroreflected both lasers for the three Raman beams, which minimized AC Stark shifts due to Raman beam misalignments, since the intensity ratio between the beams was chosen such that the AC Stark shifts approximately cancel[†].

In addition to the effects mentioned above, we investigated the dependence on the transverse cooling alignment, misalignment of the incident or retroreflected Raman beams, Raman injection, room temperature, and atomic source flux and velocity distribution. Sensitivity to certain systematic effects such as Raman beam misalignment must be rechecked now that the Raman beam delivery has been improved by the addition of the fibre and the two-beam retroreflection. We observed a correlation between the phase drift and atomic beam parameters that is not yet understood and requires further study.

We measured the rotational noise of the optical table for different methods of suspension. With the table floating on pneumatic vibration isolation legs (Newport #I-2000), it had a pronounced rotational resonance at 1.7 Hz, and when resting on unfloated legs, this was replaced by rotational noise at ~12 Hz. The best performance for long-term studies was obtained by removing the legs from the optical table and resting the table close to the floor on ~5 cm high machined blocks sandwiched by 3 mm thick neoprene rubber sheets. This increased vertical vibration, but greatly reduced rotational noise and angular drift.

[†] Note that perfect AC Stark shift cancellation cannot be achieved both before and after the retroreflection AOM shift, since the intensity ratio needed for cancellation depends on the global detuning.

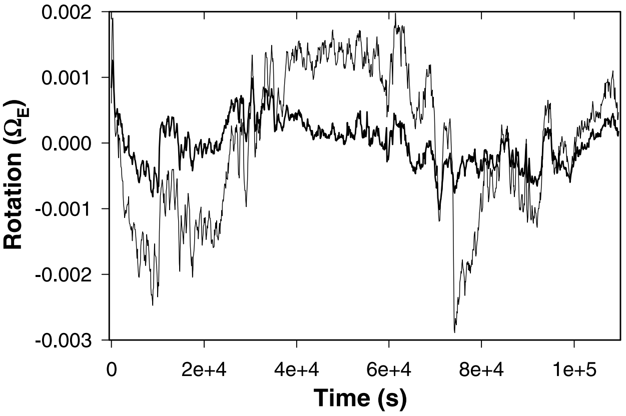

Figure 4. Preliminary long-term stability results. The Raman beams were fibre coupled with active intensity stabilization, and the optical table was resting on the floor. Phase modulation at 3.2 Hz was used with 100 samples per period, and the rotation phase was extracted using nonlinear curve fits. Each point plotted represents 60 s of data. The raw data are plotted as a thin curve. The thicker curve is the same data after normalizing by the oven flux, which was correlated to the rotation phase shift for reasons not fully understood. (The oven flux is determined by the amplitude of the phase modulation oscillations.)

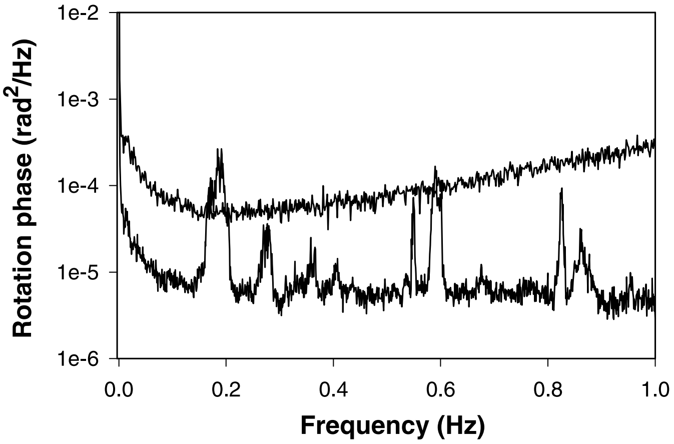

Figure 5. Power spectral density of rotation phase data. The bottom trace corresponds to the data of figure 4, taken with fibre-coupled and intensity-stabilized Raman lasers, with the optical table resting on the floor and 3.2 Hz phase modulation for data acquisition. The top trace shows previous data taken with the optical table floating, without fibre-coupling or intensity stabilization for the Raman beams, and using 48 Hz phase modulation for data acquisition. The increasing slope of the top trace is due to the floating table rotational resonance at 1.7 Hz.

5.3. Long-term stability results

The characterization of the long-term stability of the instrument is still underway, and we believe that a significant improvement can be made by identifying correlations between the rotation phase drift and various atomic beam and laser alignment parameters. Preliminary long-term stability data are shown in figure 4. These data were taken with the fibre-optic Raman delivery and intensity stabilization described in section 5.2. Also, on multiple runs, we observed a correlation between the rotation phase shift and the amplitude of the phase modulated signal from one atomic beam. The phase modulation amplitude is proportional to the oven flux, but may coincide with other changes in the velocity distribution and therefore requires further study. These data represent worst-case instrument performance, since we have no independent knowledge of the rotational stability of our laboratory. We plan to acquire data for longer times to test for environmental disturbances with 24 h periodicity. Figure 5 compares the Fourier power spectral density of the data before and after implementing the stability improvements described in the previous section.

6. Conclusion

In summary, we have constructed a gyroscope using atom interferometry that has a short-term sensitivity of 6×10^{-10} rad s^{-1} $\mathrm{Hz}^{-1/2}$. The device uses counterpropagating atomic beams to distinguish rotation from acceleration, determine absolute zero rotation rate, and for common-mode rejection. Adding independent frequency shifts to the Raman beams allows rotation compensation and synchronous detection schemes. Long-term stability testing is still underway, and we expect substantial improvements can be made with modest changes to our apparatus.

One approach to improving long-term performance is to periodically reverse the interferometer area. Switching the direction of the Raman k-vectors reverses the direction of the momentum kick to the atoms as well as the sign of the vector area associated with the loop. Although the Sagnac phase shift changes sign, many other potential sources of systematic shifts remain unchanged. This scheme is currently being implemented.

In the near future, we hope to reduce instrument noise to achieve shot-noise-limited performance, yielding a factor of three improvement in sensitivity. Multiple-pulse beamsplitting schemes could also be used to increase the enclosed area and sensitivity of the interferometer. With improved sensitivity, we hope to increase the integration time and observe fluctuations in the Earth's rotation rate. Long-term plans include the development of a compact and portable apparatus suitable for field use. Adding two Raman π pulses to our present apparatus would allow switching to and from a figure-of-eight interferometer geometry, in which case the apparatus could also measure gravity gradients. Finally, construction of a longer interferometer could make poorly known Earth rotation fluctuations at the $1 \times 10^{-9}\Omega_{\mathrm{E}}$ level accessible, and might be used for a test of general relativity.

Acknowledgments

This work has been funded by grants from NASA, NIST, NSF and ONR.

References

[1] Gustavson T L, Bouyer P and Kasevich M A 1997 *Phys. Rev. Lett.* **78** 2046–9

[2] Stedman G E 1997 *Rep. Prog. Phys.* **60** 615–87

[3] Werner S A, Staudenmann J L and Colella R 1979 *Phys. Rev. Lett.* **42** 1103–6

[4] Riehle F, Kisters T, Witte A, Helmcke J and Bordé C J 1991 *Phys. Rev. Lett.* **67** 177–80

[5] Lenef A *et al* 1997 *Phys. Rev. Lett.* **78** 760–3

[6] Hasselbach F and Nicklaus M 1993 *Phys. Rev.* A **48** 143–51

[7] Rowe C H *et al* 1999 *Appl. Opt.* **38** 2516–23

[8] Boynton P and Newman R 1999 *Symp. on Experimental Gravitation (Uzbekistan)*

[9] Lense J and Thirring H 1918 *Phys. Z.* **19** 156

[10] Ciufolini I, Pavlis E, Chieppa F, Fernandes-Vieira E and Pérez-Mercader J 1998 *Science* **279** 2100–3

[11] Everitt C W F 1987 *Near Zero: New Frontiers of Physics* (San Francisco, CA: Freeman) p 570

[12] Buchman S *et al* 1996 *Class. Quantum Grav.* A **13** 185–91

[13] Cerdonio M, Prodi G A and Vitale S 1988 *Gen. Rel. Grav.* **20** 83–7

[14] Gustavson T L, Bouyer P and Kasevich M A 1998 *Methods for Ultrasensitive Detection* (*Proc. SPIE* **3270**) ed B L Fearey pp 62–9

[15] Gustavson T L 2000 Precision rotation sensing using atom interferometry *PhD Thesis* Stanford University

[16] Kasevich M *et al* 1991 *Phys. Rev. Lett.* **66** 2297–300

[17] Young B, Kasevich M and Chu S 1997 *Atom Interferometry* ed P R Berman (New York: Academic) pp 363–406

[18] Bouyer P, Gustavson T L, Haritos K G and Kasevich M A 1996 *Opt. Lett.* **21** 1502–4

[19] Kasevich M and Chu S 1991 *Phys. Rev. Lett.* **67** 181–4

[20] Kasevich M and Chu S 1992 *Appl. Phys.* B **54** 321–32

[21] Neutze R and Hasselbach F 1998 *Phys. Rev.* A **58** 557–65

[22] Bordé C J 1997 *Atom Interferometry* ed P R Berman (New York: Academic) pp 257–92

[23] Bordé C J and Lämmerzahl C 1999 *Ann. Phys., Lpz.* **8** 83–110

[24] Storey P and Cohen-Tannoudji C 1994 *J. Physique II* **4** 1999–2027

[25] Bordé C J 1992 *Laser Spectroscopy X* ed M Ducloy, E Giacobino and G Camy (Singapore: World Scientific) pp 239–45

[26] Feynman R P and Hibbs A R 1965 *Quantum Mechanics and Path Integrals* (New York: McGraw-Hill)